

Spintronics Based Terahertz Sources

Maorong Wang ^{1,2}, Yifan Zhang ^{1,2}, Leilei Guo ^{1,2}, Mengqi Lv ^{1,2}, Peng Wang ^{1,2,*} and Xia Wang ^{2,3}¹ College of Mathematics and Physics, Qingdao University of Science and Technology, Qingdao 266061, China² Advanced Optoelectronic Materials and Technologies Engineering Laboratory of Shandong, Qingdao 266061, China³ School of Physics and Technology, Jinan University, Jinan 250024, China

* Correspondence: pwang@qust.edu.cn

Abstract: Terahertz (THz) sources, covering a range from about 0.1 to 10 THz, are key devices for applying terahertz technology. Spintronics-based THz sources, with the advantages of low cost, ultra-broadband, high efficiency, and tunable polarization, have attracted a great deal of attention recently. This paper reviews the emission mechanism, experimental implementation, performance optimization, manipulation, and applications of spintronic THz sources. The recent advances and existing problems in spintronic THz sources are fully present and discussed. This review is expected to be an introduction of spintronic terahertz sources for novices in this field, as well as a comprehensive reference for experienced researchers.

Keywords: spintronics; terahertz sources; polarization manipulation; femtosecond laser

1. Introduction

Terahertz (THz) radiation is located between the microwave band and the infrared band on the electromagnetic spectrum and its frequency range is defined as 0.1–10 THz [1]. Terahertz waves cover the characteristic spectrum of semiconductors, plasmas, biological macromolecules, cosmic radiation, etc. [2–4], and they also have the advantages of a wide frequency band, low photon energy, high penetration, and fingerprinting. Therefore, terahertz technology has a wide range of applications in material characterization, wireless communication, radar and imaging, medical diagnosis, and security detection [5–9].

A high-quality terahertz source is an indispensable core component for the application of terahertz technology. Currently, most broadband THz sources are driven by femtosecond laser pulses to generate terahertz pulses. Typical THz emitters based on ultrafast laser pumping mainly include electro-optic crystals (such as ZnTe, LiNbO₃, and GaP) [10–12], the photoconductive antenna [13,14], and air plasma [15,16], etc., but they have certain bottlenecks in terms of bandwidth, cost, or simplicity. Due to material constraints, the bandwidth of solid-state THz emitters is generally limited to a range of a few THz. For example, the spectral width of the ZnTe electro-optic crystal is only up to 3 THz [17]. THz sources based on air plasma can cover the entire THz window, but the disadvantage is that the gas ionization process usually requires high-energy femtosecond pulses in the order of 0.1 mJ [18]. The new ultra-wideband terahertz source with high efficiency and low cost has a strong application demand in the fields of material characterization and biomedical detection.

The terahertz sources described above only utilize the charge degree of electrons, not the spin degree of electrons. In recent years, the development of spintronics and femtosecond magnetism has opened up a new avenue for the development of terahertz radiation sources that utilize ultrafast demagnetization and spin-to-charge conversion. In 2004, Beaupaire et al. [19] first observed weak terahertz radiation generated by femtosecond laser irradiation on ferromagnetic films and interpreted it as magnetic dipole radiation during ultrafast demagnetization. In 2013, Kampfrath et al. [20] introduced the spin-to-charge conversion mechanism using the inverse spin-Hall effect (ISHE) in ferromagnetic/nonmagnetic



Citation: Wang, M.; Zhang, Y.; Guo, L.; Lv, M.; Wang, P.; Wang, X. Spintronics Based Terahertz Sources. *Crystals* **2022**, *12*, 1661. <https://doi.org/10.3390/cryst12111661>

Academic Editor: Martin Dressel

Received: 15 October 2022

Accepted: 14 November 2022

Published: 18 November 2022

Publisher's Note: MDPI stays neutral with regard to jurisdictional claims in published maps and institutional affiliations.



Copyright: © 2022 by the authors. Licensee MDPI, Basel, Switzerland. This article is an open access article distributed under the terms and conditions of the Creative Commons Attribution (CC BY) license (<https://creativecommons.org/licenses/by/4.0/>).

heterojunctions to improve the performance of terahertz radiation, which achieved great success. This novel spintronics-based terahertz source presents unprecedented advantages, such as ultra-broad bandwidth (up to 30 THz), simple structure, low fabrication cost, and tunable polarization [21]. More importantly, the femtosecond pulse energy required for this new scheme is in the order of nJ [21], which can be provided by a simple femtosecond oscillator. In this brief review, we first introduce the emission mechanism and experimental implementation of spintronic THz emitters (STE). Then, the recent advances made to optimize and manipulate STEs are presented. Finally, this paper further discusses the application of STEs.

2. Mechanism of THz Emission from Spintronic THz Sources

According to classical electromagnetic theory, the generation of THz radiation requires a time-dependent charge-current density J . The resulting THz radiation can be described by the wave equation of the electric field E based on Maxwell's equations [22]:

$$\nabla^2 E + \omega^2 u_0 \varepsilon E = u_0 i \omega J \quad (1)$$

where ω is the angular frequency, ε is the permittivity, and u_0 is the permeability in vacuum. Further, the total J can be separated into three parts:

$$J = J_f + \frac{\partial P}{\partial t} + \nabla \times M \quad (2)$$

where J_f is the free current density, P is electric polarization, and M is the magnetization. According to the three terms in Equation (2), three mechanisms can contribute to THz radiation. Commonly, two cores based on femtosecond lasers to produce terahertz radiation are photoconductive antennas and electro-optic crystals, where transient photocurrents in semiconductors or nonlinear optical responses of bound electrons are induced by ultrashort optical pulses. The third term represents terahertz emissions associated with magnetization, such as those caused by ultrafast demagnetization [23–25] and ultrafast-spin reorientation transition [26–29]. Because of the very weak terahertz emission directly generated by magnetic dipole radiation, it is often used to study ultrafast-magnetization dynamics.

In contrast to the photoconductive antennas and electro-optic crystals, the core mechanism of STE is the conversion from the ultrafast-spin current to charge current, which yields the J_f term in Equation (2). Figure 1 shows a schematic diagram of STE. A typical STE is a heterojunction composed of ferromagnetic metal (FM) and normal metal (NM) layers with thicknesses of several nanometers. The generation of terahertz radiation based on STE generally involves the following four mechanisms. (1) Using femtosecond laser pulses to irradiate the FM/NM heterostructure to excite spin-up and spin-down non-equilibrium carriers in the FM layer. (2) The non-equilibrium carriers diffuse to the adjacent NM layer. Due to the significant difference in the speed of the spin-up and spin-down carriers, an ultrafast-spin (polarized) current j_s is formed and injected into the NM layer from the FM layer. (3) Due to the strong spin-orbit coupling in the NM layer, the ultrafast-spin current j_s entering the NM layer is converted into a transient charge current j_c . (4) The ultrafast j_c emits THz radiation according to Equation (1). Phenomenologically, the spin-to-charge conversion can be described by the following equation [20]:

$$j_c = \gamma j_s \times M / |M| \quad (3)$$

where γ represents the efficiency of spin-charge conversion and M represents the magnetization of the FM layer. Since j_c is always perpendicular to M , the polarization of the generated THz pulses is always perpendicular to M and can be manipulated by an external magnetic field H_{ext} .

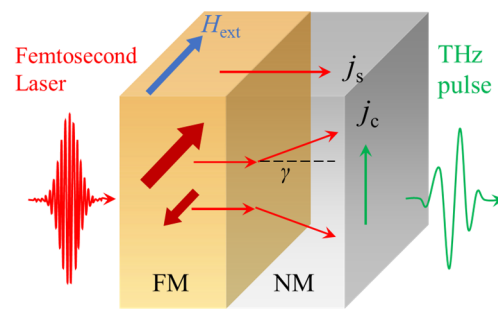


Figure 1. Schematic diagram of the spintronic THz emitter.

There are two primary mechanisms for the core spin-to-charge conversion process in STE: ISHE [30–33] and the inverse Rashba Edelstein effect (IREE) [34,35]. For the ISHE, γ is accordingly called the spin-Hall angle. Both ISHE and IREE are based on spin-orbit coupling. ISHE is a bulk effect that exists in various materials (such as Pt, W, and other heavy metals), while IREE is an interface effect that mainly exists at the interface of metal heterostructures (such as Ag/Bi interface, Cu/Bi interface, etc.), topological insulator surface states, two-dimensional electron gas, etc. The ISHE has been a very active research direction in spintronics during the past 10 years. STE studies using heavy metals as the NM layer were mainly based on the ISHE mechanism early. In 2018, Jungfleisch et al. [36] and Zhou et al. [37] reported the results of broadband terahertz radiation based on the IREE mechanism, respectively. Moreover, the studies by Zhou et al. [37] showed that the terahertz radiation generated by IREE and ISHE can be superimposed to improve the emitter efficiency.

In addition, there are also spintronic THz emissions from magnetic films that are not based on the above-mentioned typical mechanisms and FM/NM structures. The Kampfrath research group [38] observed THz pulses generated by the injection of ultrafast pure-spin currents into heavy metal Pt from the ferromagnetic insulator (FI) YIG layer based on the spin Seebeck effect [39,40]. Recently, Qiu et al. [41] demonstrated that laser-induced transient magnetization of an antiferromagnetic (AFM) NiO layer at zero magnetic fields could inject ultrafast-spin currents into adjacent heavy metal layers. Zhang et al. [42] even reported THz emission from a single-layer ferromagnet via the anomalous Hall effect. Although their emission intensity is inferior to the FM/NM devices, they provide new ideas for the design of STE.

3. Experimental Setup for Spintronic THz Sources

3.1. Terahertz Time-Domain Spectroscopy

The experimental study of spintronic terahertz sources mainly relies on the terahertz time-domain spectroscopy (THz-TDS) [43]. A typical THz-TDS experimental setup is shown in Figure 2. The energy of femtosecond laser will be divided into two parts: signal light path and reference light path by a beam splitter; the optical path difference between the two paths is controlled by an optical delay line. The pump beam excites the THz source to generate a THz wave and off-axis parabolic mirrors are used for collimating and focusing the THz wave. Finally, the THz wave and the probe beam are overlapped on an electro-optic (EO) crystal. The refractive index of the EO crystal will change proportionally to the strength of the THz electric field via the linear EO effect, which can be sampled by the time-delayed probe beam. Therefore, the time-domain waveform of the THz electric field can be measured indirectly and the corresponding frequency domain spectrum can be obtained by Fourier transform. The THz signal $S(t)$ measured directly by the EO crystal is the convolution of the THz electric field $E_{\text{det}}(t)$ and the response function $h(t)$. One can first calculate $h(t)$ through the parameters of the EO crystal and sampling pulse and then numerically calculate $E_{\text{det}}(t)$.

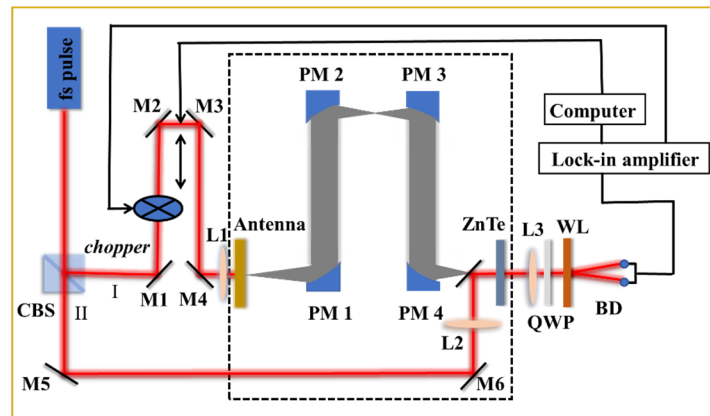


Figure 2. Schematic diagram of the terahertz time-domain spectroscopy system.

3.2. Typical THz-Emission Signals from Spintronic THz Sources

A typical THz-emission signal from the metallic spintronic Fe/Pt heterostructure in the study by Torosyan et al. [43] is shown in Figure 3. First, the polarization of the THz signal was perpendicular to the sample magnetization M and reversed upon reversing M by the magnetic field. Second, the polarity of the THz signal is reversed when the bilayer order is reversed, because j_s flowing from FM to NM changes its sign. These results are consistent with Equation (3) for the spin-charge conversion. The bandwidth of the emission spectrum of Fe/Pt in their study is up to 8 THz, which was limited by the GaAs photoconductive antenna detector and the pulse length of the pump laser. Seifert et al. [21] demonstrated that with different detectors (e.g., GaP electro-optic crystal) and shorter pump pulses, wider bandwidths up to 30 THz can be obtained. Notably, they used a femtosecond laser with a repetition rate of 75 MHz for THz generation, and the energy of each pumping pulse is in the order of nJ.

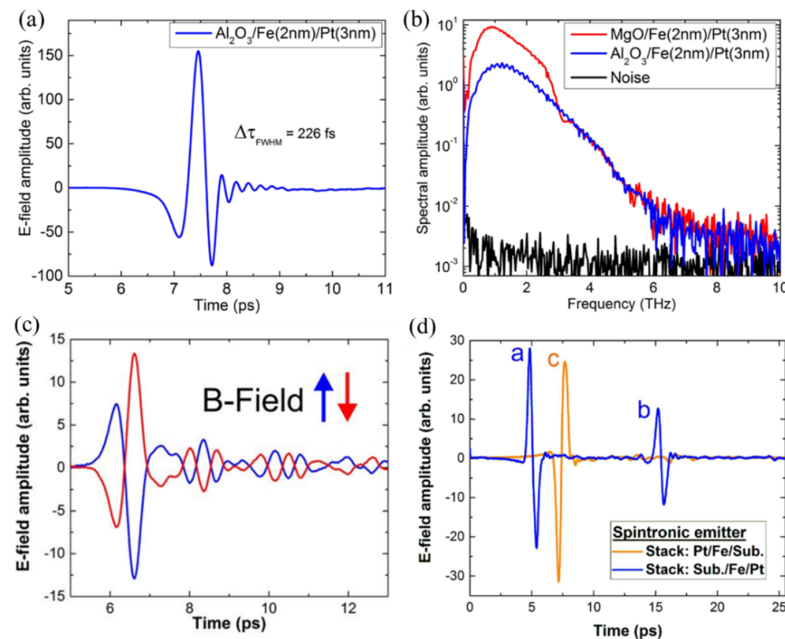


Figure 3. Typical THz-emission signals from spintronic FM/NM heterostructures. (a) Terahertz signal waveforms obtained from a Fe/Pt bilayer. (b) Fourier spectra of (a). (c) THz pulses for opposite sample magnetizations. (d) THz pulses for reversed bilayer order. It is reproduced under the terms of a Creative Commons Attribution 4.0 License [44] Copyright 2018, the Authors, published by Springer Nature.

4. Performance Optimization of Spintronic THz Sources

In recent years, several research groups [44–50] have used various methods to improve the emission efficiency and power of STE to the level of commercial THz pulse sources. Nenno et al. [51] constructed a roadmap of THz emission from magnetic films containing the most important physical parameters that can influence the efficiency of STEs (see Figure 4). Here, we mainly focus on optimizing the material properties and thicknesses of the FM and NM layers, as well as the optical and geometrical design of the STE, which have more significant impacts on the THz emission efficiency.

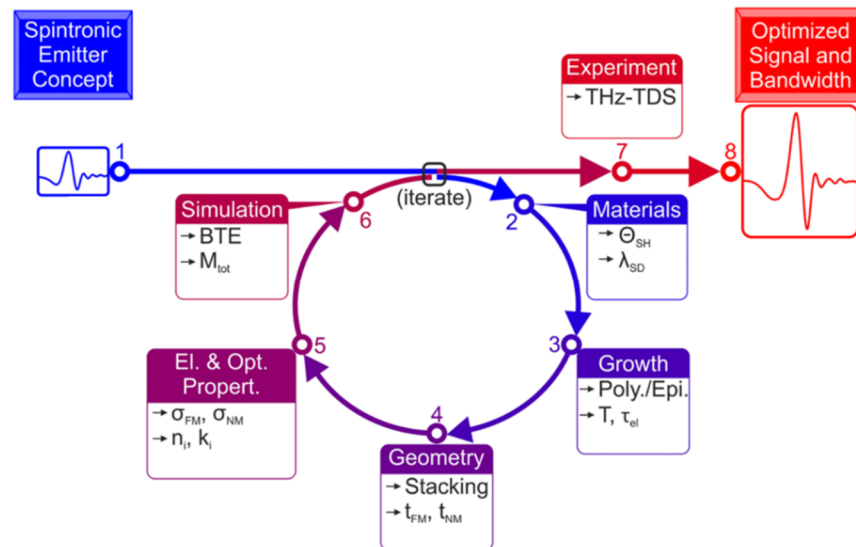


Figure 4. Roadmap to efficient STEs, which includes materials, growth quality, film thickness, geometry, electrical and optical parameters, and theoretical simulations. Reproduced under the terms of a Creative Commons Attribution 4.0 Licence [51] Copyright 2019, The Authors, published by Springer Nature.

4.1. Optimizing Materials

According to Equation (3), the spin-Hall angle γ of NM materials has a significant impact on the performance of STE. Seifert et al. [21] systematically studied the performance of STE based on different NM materials, including Cr, Pd, Ta, W, Ir, Pt₃₈Mn₆₂, and Pt. They found that the amplitude and polarity of the THz field strongly depend on the chosen NM material. For example, Pt is an order of magnitude stronger than Ta or Ir, while W and Pt have opposite polarities because of the opposite signs of γ . The trend of THz amplitudes with respect to NM materials is in good agreement with the calculated spin-Hall conductivity. Related works [52–56] also studied NM materials, such as Au, Ru, Al, IrMn₃, and Mn₂Au. At present, Pt is still the best choice for preparing NM layers, owing to the lesser effect on the THz amplitude for STEs. Co₄₀Fe₄₀B₂₀ is slightly higher than other FM metals, such as Fe, Co, Fe-Co alloys, and Ni₈₁Fe₁₉, while the efficiency of pure Ni-based STEs is rather low. Recent works [57–59] have also investigated STEs based on half-metallic FM materials, such as Heusler alloys, which are believed to have large spin polarization. The experimental results show that the spin-current generation efficiency of half-metallic FMs in STEs can reach that of typical 3D-transition-metal FMs, such as Fe, but not be higher. Nenno et al. [51] introduced defect engineering to modify the STE performance by controlling the growth quality of the NM and FM films, which suggest that the THz bandwidth can be controlled by introducing defects into the sample, but at the expense of reducing the THz amplitude.

Traditional NM materials are discussed above. Topological materials have promising properties for their use in STEs, such as large spin-to-charge conversion efficiencies and topological surface state [60,61]. In 2018, Wang et al. [62] first used the FM/Bi₂Se₃ heterojunction to generate THz radiation and attributed it to the combination of the ISHE

and IREE mechanisms. However, its THz emission intensity is quite small compared with traditional FM/NM heterostructures. Tong et al. [63] enhanced the THz emission intensity by inserting a meticulously designed thickness of heavy metal layer between the FM and topological insulator layers. Park et al. [64,65] further demonstrated the important role of inversion symmetry breaking and topological surface states in the performance of topological material-based STEs and observed THz emissions larger than those of Pt in the topologically nontrivial semimetal $\text{Bi}_{1-x}\text{Sb}_x$ films. Recently, the THz emission of heterojunctions formed by the combination of two-dimensional materials and FM layers, even by solution processing, has been realized [66,67], which provides another direction for the integration of STEs.

4.2. Optimizing Thickness

The THz emission efficiency depends strongly on the thickness of each layer in the FM/NM heterostructures. The optimal thickness of the NM layer depends, in particular, on the spin diffusion length λ_{NM} . Several studies [21,44,68] have shown that when the thickness of the NM layer is greater than the spin diffusion length, the THz signal decreases with the thickness. As for the FM layer, because of the finite spin propagation length λ_{FM} inside the FM layer, additional FM thickness far from the FM/NM interface does not contribute to the THz emission. Below a dead-layer thickness about 0.5 nm [24], the change in the magnetic order of the FM layer also reduces the THz emission. Studies of the thickness variation in the NM and FN layers have shown that the optimal thickness for both layers is around 1–4 nm [21,37,44,50,68].

4.3. Optimizing Structures

At present, the optimization of the structure mainly focuses on “sandwich-like” structures, antenna-coupled structures, current-enhanced and nano plasmonic resonance enhanced structures shown in Figure 5.

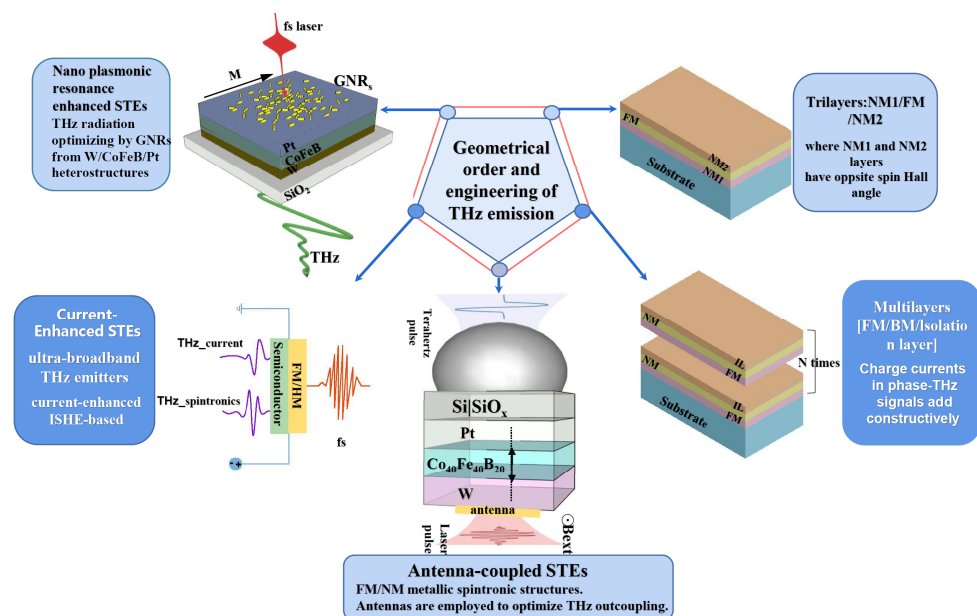


Figure 5. Structural optimization of the STE.

To further utilize the backward spin current, Seifert et al. [21] first introduced another NM layer to the left of the FM layer, making a triple-layer structure of $\text{W}/\text{Co}_{40}\text{Fe}_{40}\text{B}_{20}/\text{Pt}$. Due to the inverse sign of the spin-Hall angles of W and Pt, the spin-Hall currents j_c of W and Pt layers are in the same direction, thus, enhancing the THz emission. The experimental results show that the THz amplitude of the $\text{NM}_1/\text{FM}/\text{NM}_2$ trilayers is almost twice that of

the bilayers under the same total thickness and exceeds that of standard THz sources, such as ZnTe, GaP, and photoconductive antennas (shown in Figure 5).

Feng et al. [69] studied the structural unit of the dielectric layer/NM₁/FM/NM₂ and repeated the unit to form multiple structures of (dielectric layer/NM₁/FM/NM₂)_n. The dielectric layer can effectively suppress the reflection and transmission of laser light, thereby increasing its absorption rate in the metal film and effectively improving the THz emission efficiency of the device. Compared with the standard single-period STE, the generation efficiency of the multiple structure with $n = 2$ is increased by 1.7-times. Similar results were also reported by Herapath et al. by integrating the W/CoFeB/Pt emitter with a dielectric lattice TiO₂/SiO₂. Recently, Jin et al. [70] utilized a cascade design of STEs fabricated on a flexible polyethylene terephthalate (PET) substrate and yielded a 1.55-times amplification compared to a single PET/STE.

Nandi et al. [71] coupled the STE with an on-chip antenna and the measured THz intensity of the antenna-coupled structure was increased to 2.42-times that of the pure film structure. Shahriar et al. [72] coupled a waveguide-fed horn antenna with the STE to increase the emission power. In addition, Hoppe et al. [73] combined the STE with a metallic waveguide to achieve on-chip THz emission and electrical detection of THz signals.

Chen et al. [74] constructed a novel current-enhanced STE combined with semiconductor materials, which realized the superposition of the ISHE and the conventional photocurrent mechanism. The experimental results show that the intensity of the generated THz spectrum in the low-frequency band (0.1–0.5 THz) is enhanced by 2–3 orders of magnitude when the current is applied. Additionally, surface plasmonic resonance was also introduced to improve the performance for the STE by Liu et al. [75]. They reported that gold nanorod (GNR) plasmonic resonance could effectively increase the terahertz emission of W/CoFeB/Pt heterostructures by 140%.

5. Manipulation of Terahertz Emission by Spintronic THz Sources

One of the unique properties of STE is tunable polarization. According to Equation (3), the polarization of the emitted THz pulses from STEs is always perpendicular to the magnetization M of the FM layer. Therefore, the polarization can be manipulated by manipulating M with magnetic or electric fields. In fact, due to the cross product of M and j_c , the amplitude of the THz emission can also be manipulated by manipulating the magnitude and direction of M .

5.1. Magnetic-Field Manipulation

The most intuitive idea is to place the STE in straight magnetic field lines between two polar-aligned permanent magnets to generate linearly polarized THz radiation and to rotate the direction of the polarization by rotating the permanent magnets. Hibberd et al. [76] further demonstrated that a quadrupole-like polarization profile could be generated by placing the STE between two magnets of opposing polarity, as schematically illustrated in Figure 6a. They, thus, proposed a proof-of-principle concept that magnetic-field patterns can be applied to tailor the spatial polarization profile of THz radiation from STE. In addition to spatial modulation of polarization, temporal modulation of polarization can also be achieved by magnetic fields. In a recent study, Gueckstock et al. [77] performed polarity modulation of THz pulses from STE at a rate of 10 kHz and with a contrast exceeding 99% using a harmonic magnetic field, as shown in Figure 6b.

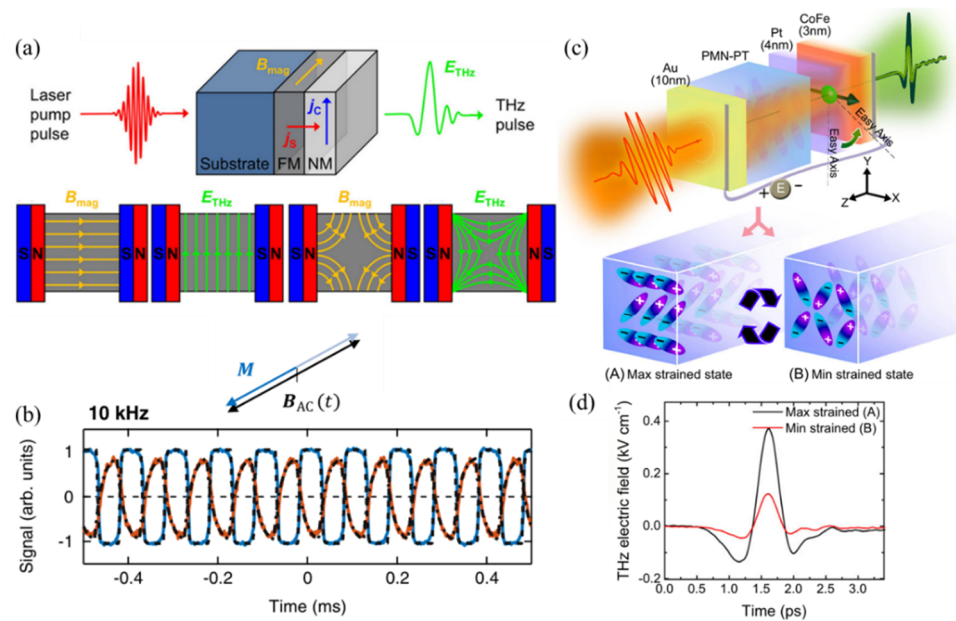


Figure 6. Magnetic-field and electric-field manipulation of THz emission from STE. (a) Schematic diagram of manipulating THz polarization by the magnetic field. Reproduced under the terms of a Creative Commons Attribution 4.0 Licence [76] Copyright 2019, the Authors, published by AIP Publishing. (b) Modulation of the THz polarity at kHz rates using a harmonic magnetic field. Reproduced under the terms of the OSA Open Access Publishing Agreement [77] Copyright 2021, Optica Publishing Group. (c) Schematic and (d) results of manipulating the THz emission by electric field. Reproduced under the terms of a Creative Commons Attribution 4.0 Licence [78] Copyright 2022, the Authors, published by Springer Nature.

Research [79,80] by Wu et al. was devoted to shaping the THz polarization of STE from linear to circular. They demonstrated that an elliptically polarized THz pulse could be easily produced by applying curved magnetic-field distributions. They also demonstrated the generation of circularly polarized THz waves in a cascade configuration consisting of two spatially separated STEs with an orthogonal external magnetic field and nearly equal amplitude and 90° phase difference.

5.2. Electric-Field Manipulation

Compared with magnetic-field manipulation, electric-field manipulation is more adaptable and more suitable for integration. Manipulating the THz emission from STE with electric fields is essentially achieved by an electric field manipulating the magnetization M in the FM layer. A typical approach is to integrate the STEs on piezoelectric materials, such as PMN-PT, and utilize magnetoelectric coupling to control the magnetization, as schematically illustrated in Figure 6c. Figure 6d shows the electric-field manipulation results of THz pulses emitted from STEs on PMN-PT by Agarwal et al. [78], which indicates that the electric-field control can tune the emitted THz amplitude by up to 270%. In a similar earlier study by Cheng et al. [81], a THz amplitude modulation depth of 69% was achieved. The study by Khusyainov et al. [82] was more concerned with polarization control via an electric field and the maximum angle of THz polarization rotation by the electric field was observed to be 66° .

6. Applications of Spintronic THz Sources

Spintronic THz sources have the advantages of ultra-broadband, controllable polarization, low cost, easy handling and integration, etc., and, thus, enable a variety of applications. In the following, we will focus their applications in broadband THz spectroscopy and THz imaging. More application scenarios for STEs will emerge as time goes on.

6.1. Broadband THz Spectroscopy

The spectral bandwidth of STEs is up to 30 THz, thus, enabling ultra-broad spectral measurements of various materials. In earlier works, Seifert et al. [21] measured the THz transmission spectrum of 7.5 μm thick polytetrafluoroethylene (PTFE) using an ultra-broadband STE-based THz-TDS and observed distinct resonant absorptions at 6, 15, and 18 THz. In a subsequent work [83], they used the amplified Ti: sapphire laser system to pump an STE with a diameter of 7.5 cm and a strong THz electric field up to 0.3 MV/cm was successfully generated. Such strong THz waves with ultra-short pulse width can be used to study THz nonlinear optical effects, such as the THz Kerr effect of the diamond.

Milot et al. [84] used an STE-based THz spectroscopy system to measure the THz-frequency photoconductivity of perovskite samples as a function of the doping density and temperature. In a recent work [70], cascaded PET/STE was used to perform a spectroscopic measurement of riboflavin with a high signal-to-noise ratio. The above results were in the far-field-type approach of THz-TDS. In near-field-type approaches, Bai et al. [85] realized a monolithic THz emission biosensor by integrating metamaterials with STE, and the THz sensing of Hela cells and Pseudomonas was demonstrated. Using water as the test liquid, Balos et al. [86] demonstrated an STE-based near-field THz-TDS approach for measuring the dielectric response of liquids and ascertained the dielectric loss and permittivity of water in a range of 0.3–15 THz.

Müller et al. [83] coupled STE-generated ultra-broadband (1–30 THz) THz pulses to a scanning tunneling microscope (STM) junction to form a THz-gated STM (THz-STM) (see Figure 7a), which has the potential to enable imaging of ultrafast dynamics in materials with atomic resolution. They demonstrate the suitability of STEs as a broadband source for ultrafast THz-STM, where THz voltage transients with frequencies up to 15 THz can couple to the STM junction.

In addition, THz emission spectroscopy from STEs is also an excellent tool for studying the spin–charge conversion and related phenomena [87]. Compared to traditional transport methods, this all-optical contact-free approach can extract spin-Hall angles and spin current relaxation lengths with large sample throughput without any micro-structuring [69].

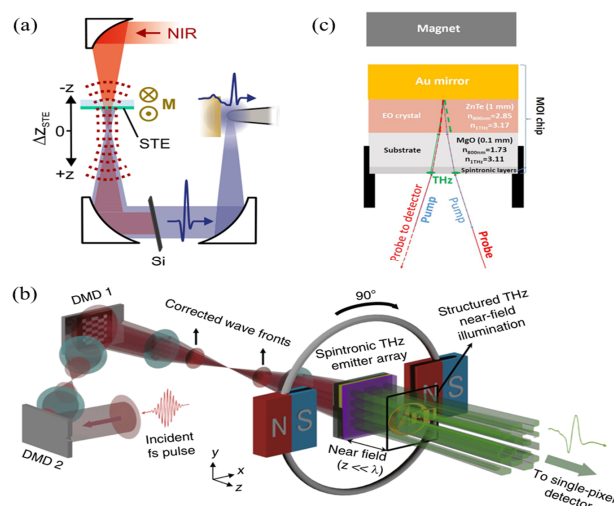


Figure 7. Applications of STEs. (a) Ultra-broadband THz-STM setup (NIR: near-infrared). Reproduced under the terms of a Creative Commons Attribution 4.0 Licence [88] Copyright 2020, the Authors, published by ACS Publications. (b) Ghost spintronic THz-emitter-array microscope (DMD: digital micromirror device). Reproduced under the terms of a Creative Commons Attribution 4.0 Licence [89] Copyright 2020, the Authors, published by Springer Nature. (c) THz Magneto-optic sensor/imager. Reproduced under the terms of a Creative Commons Attribution 4.0 Licence [90] Copyright 2020, the Authors, published by Springer Nature.

6.2. THz Imaging

Because it can be tightly attached to objects at the nanoscale, the STE has significant advantages in THz near-field imaging. Chen et al. [84] demonstrated for the first time THz super-resolution near-field imaging using a W/Fe/Pt STE array, see Figure 7b. In their experiments, the STE array was illuminated with a spatially structured pump beam and the emitted THz waves were recorded by EO detection after passing through the imaging object and an inversion algorithm was used to reconstruct the image of the object. Guo et al. [91] examined the feasibility of integrating W/CoFeB/Pt heterostructures in a laser THz emission microscopy (LTEM) technology and proposed a new conception of STE microscopy (STEM). In a recent work, Stiewe et al. [92] further achieved STE-based super-resolution (up to 5 μm) THz spectral imaging.

Agarwal et al. [93] observed the linear relationship between the STE-generated THz pulse amplitude and the magnetization of the FM layer in the STE. Therefore, the hysteresis loop of the FM layer can be obtained by measuring the change in the THz amplitude with the magnetic field. Taking advantage of the above feature, Bulgarevich et al. [85] proposed a new type of magneto-optic imaging (MOI) based on STEs. The structure of the THz MOI sensor is STE layers/MgO substrate/EO crystal/Au mirror, as shown in Figure 7c. With this simple sensor and a THz-TDS in reflection-type geometry, they could record the magnetic field distribution of permanent magnets near the sensor surface with a sensitivity of mT.

7. Conclusions

This paper reviews spintronics-based THz sources, including their implementation, optimization, manipulation, and applications. The THz radiation produced by the STE can meet the needs of many applications, such as spectroscopy and imaging. Although the research on STEs has made remarkable progress, there are still some problems to be solved. For example, the generated THz intensity by a femtosecond pulse is still weaker than that of a photoconductive antenna; the acquisition speed of THz super-resolution near-field imaging is quite slow; and the sensitivity of magnetic field imaging is much lower than typical MOI. In addition, unlike other THz sources, such as ZnTe crystal, currently, the STE can only be used for THz generation but not for THz detection. To solve these problems, it is necessary to comprehensively utilize multiple disciplines, such as optics, terahertz science, and spintronics, to further improve the efficiency and practicality of STEs. This review is expected to provide a reference for researchers and help push the progress of spintronics-based THz sources.

Author Contributions: Data curation, Y.Z.; formal analysis, L.G. and M.L.; investigation, X.W.; project administration, M.W.; writing—original draft, P.W. All authors have read and agreed to the published version of the manuscript.

Funding: This research was funded by the National Natural Science Foundation of China (Grant No. 61905127, Grant No. 11904194) and the Open Fund of the Key Laboratory of Optoelectronic Information Technology Education (Tianjin University) (Grant No. 2022KFKT015).

Institutional Review Board Statement: Not applicable.

Informed Consent Statement: Not applicable.

Data Availability Statement: Not applicable.

Acknowledgments: We thank the editors for technical support.

Conflicts of Interest: The authors declare no conflict of interest.

References

1. Ferguson, B.; Zhang, X.C. Materials for Terahertz Science and Technology. *Nat. Mater.* **2002**, *1*, 26–33. [[CrossRef](#)] [[PubMed](#)]
2. Tonouchi, M. Cutting-Edge Terahertz Technology. *Nat. Photonics* **2007**, *1*, 97–105.003C003E. [[CrossRef](#)]
3. Basov, D.N.; Averitt, R.D.; van der Marel, D.; Dressel, M.; Haule, K. Electrodynamics of Correlated Electron Materials. *Rev. Mod. Phys.* **2011**, *83*, 471–541. [[CrossRef](#)]
4. Kampfrath, T.; Tanaka, K.; Nelson, K.A. Resonant and Nonresonant Control over Matter and Light by Intense Terahertz Transients. *Nat. Photonics* **2013**, *7*, 680–690. [[CrossRef](#)]
5. Hangyo, M.; Tani, M.; Nagashima, T. Terahertz Time-Domain Spectroscopy of Solids: A Review. *Int. J. Infrared Millim. Waves* **2005**, *26*, 1661–1690. [[CrossRef](#)]
6. Koenig, S.; Lopez-Diaz, D.; Antes, J.; Boes, F.; Henneberger, R.; Leuther, A.; Tessmann, A.; Schmogrow, R.; Hillerkuss, D.; Palmer, R.; et al. Wireless Sub-THz Communication System with High Data Rate. *Nat. Photonics* **2013**, *7*, 977–981. [[CrossRef](#)]
7. Federici, J.; Moeller, L. Review of Terahertz and Subterahertz Wireless Communications. *J. Appl. Phys.* **2010**, *107*, 111101. [[CrossRef](#)]
8. Pickwell, E.; Wallace, V.P. Biomedical Applications of Terahertz Technology. *J. Phys. D Appl. Phys.* **2006**, *39*, R301–R310. [[CrossRef](#)]
9. Jepsen, P.U.; Cooke, D.G.; Koch, M. Terahertz Spectroscopy and Imaging—Modern Techniques and Applications. *Laser Photon. Rev.* **2011**, *5*, 124–166. [[CrossRef](#)]
10. Rice, A.; Jin, Y.; Ma, X.F.; Zhang, X.C.; Bliss, D.; Larkin, J.; Alexander, M. Terahertz Optical Rectification from $\langle 110 \rangle$ Zinc-blende Crystals. *Appl. Phys. Lett.* **1994**, *64*, 1324–1326. [[CrossRef](#)]
11. Kawase, K.; Sato, M.; Taniuchi, T.; Ito, H. Coherent Tunable THz-wave Generation from LiNbO₃ with Monolithic Grating Coupler. *Appl. Phys. Lett.* **1996**, *68*, 2483–2485. [[CrossRef](#)]
12. Hoffmann, M.C.; Yeh, K.-L.; Hebling, J.; Nelson, K.A. Efficient Terahertz Generation by Optical Rectification at 1035 Nm. *Opt. Express* **2007**, *15*, 11706. [[CrossRef](#)] [[PubMed](#)]
13. Auston, D.H.; Cheung, K.P.; Smith, P.R. Picosecond Photoconducting Hertzian Dipoles. *Appl. Phys. Lett.* **1984**, *45*, 284–286. [[CrossRef](#)]
14. Lepeshov, S.; Gorodetsky, A.; Krasnok, A.; Rafailov, E.; Belov, P. Enhancement of Terahertz Photoconductive Antenna Operation by Optical Nanoantennas. *Laser Photon. Rev.* **2017**, *11*, 1600199. [[CrossRef](#)]
15. Zhong, H.; Karpowicz, N.; Zhang, X.C. Terahertz Emission Profile from Laser-Induced Air Plasma. *Appl. Phys. Lett.* **2006**, *88*, 261103. [[CrossRef](#)]
16. Xie, X.; Dai, J.; Zhang, X.C. Coherent Control of THz Wave Generation in Ambient Air. *Phys. Rev. Lett.* **2006**, *96*, 075005. [[CrossRef](#)] [[PubMed](#)]
17. Blanchard, F.; Sharma, G.; Razzari, L.; Ropagnol, X.; Bandulet, H.-C.; Vidal, F.; Morandotti, R.; Kieffer, J.-C.; Ozaki, T.; Tiedje, H.; et al. Generation of Intense Terahertz Radiation via Optical Methods. *IEEE J. Sel. Top. Quantum Electron.* **2011**, *17*, 5–16. [[CrossRef](#)]
18. Roskos, H.G.; Thomson, M.D.; Krefß, M.; Löffler, T. Broadband THz Emission from Gas Plasmas Induced by Femtosecond Optical Pulses: From Fundamentals to Applications. *Laser Photonics Rev.* **2007**, *1*, 349–368. [[CrossRef](#)]
19. Beaurepaire, E.; Turner, G.M.; Harrel, S.M.; Beard, M.C.; Bigot, J.Y.; Schmuttenmaer, C.A. Coherent Terahertz Emission from Ferromagnetic Films Excited by Femtosecond Laser Pulses. *Appl. Phys. Lett.* **2004**, *84*, 3465–3467. [[CrossRef](#)]
20. Kampfrath, T.; Battiato, M.; Maldonado, P.; Eilers, G.; Nötzold, J.; Mährlein, S.; Zbarsky, V.; Freimuth, F.; Mokrousov, Y.; Blügel, S.; et al. Terahertz Spin Current Pulses Controlled by Magnetic Heterostructures. *Nat. Nanotechnol.* **2013**, *8*, 256–260. [[CrossRef](#)]
21. Seifert, T.; Jaiswal, S.; Martens, U.; Hannegan, J.; Braun, L.; Maldonado, P.; Freimuth, F.; Kronenberg, A.; Henrizi, J.; Radu, I.; et al. Efficient Metallic Spintronic Emitters of Ultrabroadband Terahertz Radiation. *Nat. Photonics* **2016**, *10*, 483–488. [[CrossRef](#)]
22. Jackson, J.D. *Classical Electrodynamics*; Springer: Berlin/Heidelberg, Germany, 1999.
23. Beaurepaire, E.; Merle, J.-C.; Daunois, A.; Bigot, J.-Y. Ultrafast Spin Dynamics in Ferromagnetic Nickel. *Phys. Rev. Lett.* **1996**, *76*, 4250–4253. [[CrossRef](#)] [[PubMed](#)]
24. Huang, L.; Lee, S.-H.; Kim, S.-D.; Shim, J.-H.; Shin, H.J.; Kim, S.; Park, J.; Park, S.-Y.; Choi, Y.S.; Kim, H.-J.; et al. Universal Field-Tunable Terahertz Emission by Ultrafast Photoinduced Demagnetization in Fe, Ni, and Co Ferromagnetic Films. *Sci. Rep.* **2020**, *10*, 15843. [[CrossRef](#)] [[PubMed](#)]
25. Venkatesh, M.; Ramakanth, S.; Chaudhary, A.K.; Raju, K.C.J. Study of Terahertz Emission from Nickel (Ni) Films of Different Thicknesses Using Ultrafast Laser Pulses. *Opt. Mater. Express* **2016**, *6*, 2342. [[CrossRef](#)]
26. Kimel, A.V.; Kirilyuk, A.; Tsvetkov, A.; Pisarev, R.V.; Rasing, T. Laser-Induced Ultrafast Spin Reorientation in the Antiferromagnet TmFeO₃. *Nature* **2004**, *429*, 850–853. [[CrossRef](#)]
27. Yamaguchi, K.; Kurihara, T.; Minami, Y.; Nakajima, M.; Suemoto, T. Terahertz Time-Domain Observation of Spin Reorientation in Orthoferrite ErFeO₃ through Magnetic Free Induction Decay. *Phys. Rev. Lett.* **2013**, *110*, 137204. [[CrossRef](#)]
28. Mikhaylovskiy, R.V.; Hendry, E.; Kruglyak, V.V.; Pisarev, R.V.; Rasing, T.; Kimel, A.V. Terahertz Emission Spectroscopy of Laser-Induced Spin Dynamics in TmFeO₃ and ErFeO₃ Orthoferrites. *Phys. Rev. B* **2014**, *90*, 184405. [[CrossRef](#)]
29. Khusyainov, D.; Ovcharenko, S.; Gaponov, M.; Buryakov, A.; Klimov, A.; Tiercelin, N.; Pernod, P.; Nozdrin, V.; Mishina, E.; Sigov, A.; et al. Polarization Control of THz Emission Using Spin-Reorientation Transition in Spintronic Heterostructure. *Sci. Rep.* **2021**, *11*, 697. [[CrossRef](#)]

30. Hirsch, J.E. Spin Hall Effect. *Phys. Rev. Lett.* **1999**, *83*, 1834–1837. [[CrossRef](#)]
31. Sinova, J.; Valenzuela, S.O.; Wunderlich, J.; Back, C.H.; Jungwirth, T. Spin Hall Effects. *Rev. Mod. Phys.* **2015**, *87*, 1213–1260. [[CrossRef](#)]
32. Hoffmann, A. Spin Hall Effects in Metals. *IEEE Trans. Magn.* **2013**, *49*, 5172–5193. [[CrossRef](#)]
33. Jungwirth, T.; Wunderlich, J.; Olejnik, K. Spin Hall Effect Devices. *Nat. Mater.* **2012**, *11*, 382–390. [[CrossRef](#)] [[PubMed](#)]
34. Lesne, E.; Fu, Y.; Oyarzun, S.; Rojas-Sánchez, J.C.; Vaz, D.C.; Naganuma, H.; Sicoli, G.; Attané, J.P.; Jamet, M.; Jacquet, E.; et al. Highly Efficient and Tunable Spin-to-Charge Conversion through Rashba Coupling at Oxide Interfaces. *Nat. Mater.* **2016**, *15*, 1261–1266. [[CrossRef](#)]
35. Manchon, A.; Koo, H.C.; Nitta, J.; Frolov, S.M.; Duine, R.A. New Perspectives for Rashba Spin–Orbit Coupling. *Nat. Mater.* **2015**, *14*, 871–882. [[CrossRef](#)]
36. Jungfleisch, M.B.; Zhang, Q.; Zhang, W.; Pearson, J.E.; Schaller, R.D.; Wen, H.; Hoffmann, A. Control of Terahertz Emission by Ultrafast Spin-Charge Current Conversion at Rashba Interfaces. *Phys. Rev. Lett.* **2018**, *120*, 207207. [[CrossRef](#)] [[PubMed](#)]
37. Zhou, C.; Liu, Y.P.; Wang, Z.; Ma, S.J.; Jia, M.W.; Wu, R.Q.; Zhou, L.; Zhang, W.; Liu, M.K.; Wu, Y.Z.; et al. Broadband Terahertz Generation via the Interface Inverse Rashba-Edelstein Effect. *Phys. Rev. Lett.* **2018**, *121*, 086801. [[CrossRef](#)]
38. Seifert, T.S.; Jaiswal, S.; Barker, J.; Weber, S.T.; Rzdolski, I.; Cramer, J.; Gueckstock, O.; Maehrlin, S.F.; Nadvornik, L.; Watanabe, S.; et al. Femtosecond Formation Dynamics of the Spin Seebeck Effect Revealed by Terahertz Spectroscopy. *Nat. Commun.* **2018**, *9*, 2899. [[CrossRef](#)]
39. Uchida, K.; Takahashi, S.; Harii, K.; Ieda, J.; Koshibae, W.; Ando, K.; Maekawa, S.; Saitoh, E. Observation of the Spin Seebeck Effect. *Nature* **2008**, *455*, 778–781. [[CrossRef](#)]
40. Qu, D.; Huang, S.Y.; Hu, J.; Wu, R.; Chien, C.L. Intrinsic Spin Seebeck Effect in Au/YIG. *Phys. Rev. Lett.* **2013**, *110*, 067206. [[CrossRef](#)]
41. Qiu, H.; Zhou, L.; Zhang, C.; Wu, J.; Tian, Y.; Cheng, S.; Mi, S.; Zhao, H.; Zhang, Q.; Wu, D.; et al. Ultrafast Spin Current Generated from an Antiferromagnet. *Nat. Phys.* **2021**, *17*, 388–394. [[CrossRef](#)]
42. Zhang, Q.; Luo, Z.; Li, H.; Yang, Y.; Zhang, X.; Wu, Y. Terahertz Emission from Anomalous Hall Effect in a Single-Layer Ferromagnet. *Phys. Rev. Appl.* **2019**, *12*, 054027. [[CrossRef](#)]
43. Neu, J.; Schmuttenmaer, C.A. Tutorial: An Introduction to Terahertz Time Domain Spectroscopy (THz-TDS). *J. Appl. Phys.* **2018**, *124*, 231101. [[CrossRef](#)]
44. Torosyan, G.; Keller, S.; Scheuer, L.; Beigang, R.; Papaioannou, E.T. Optimized Spintronic Terahertz Emitters Based on Epitaxial Grown Fe/Pt Layer Structures. *Sci. Rep.* **2018**, *8*, 1311. [[CrossRef](#)] [[PubMed](#)]
45. Herapath, R.I.; Hornett, S.M.; Seifert, T.S.; Jakob, G.; Kläui, M.; Bertolotti, J.; Kampfrath, T.; Hendry, E. Impact of Pump Wavelength on Terahertz Emission of a Cavity-Enhanced Spintronic Trilayer. *Appl. Phys. Lett.* **2019**, *114*, 041107. [[CrossRef](#)]
46. Yang, D.; Liang, J.; Zhou, C.; Sun, L.; Zheng, R.; Luo, S.; Wu, Y.; Qi, J. Powerful and Tunable THz Emitters Based on the Fe/Pt Magnetic Heterostructure. *Adv. Opt. Mater.* **2016**, *4*, 1944–1949. [[CrossRef](#)]
47. Wu, Y.; Elyasi, M.; Qiu, X.; Chen, M.; Liu, Y.; Ke, L.; Yang, H. High-Performance THz Emitters Based on Ferromagnetic/Nonmagnetic Heterostructures. *Adv. Mater.* **2017**, *29*, 1603031. [[CrossRef](#)]
48. Sasaki, Y.; Suzuki, K.Z.; Mizukami, S. Annealing Effect on Laser Pulse-Induced THz Wave Emission in Ta/CoFeB/MgO Films. *Appl. Phys. Lett.* **2017**, *111*, 102401. [[CrossRef](#)]
49. Li, G.; Medapalli, R.; Mikhaylovskiy, R.V.; Spada, F.E.; Rasing, T.; Fullerton, E.E.; Kimel, A.V. THz Emission from Co/Pt Bilayers with Varied Roughness, Crystal Structure, and Interface Intermixing. *Phys. Rev. Mater.* **2019**, *3*, 084415. [[CrossRef](#)]
50. Sasaki, Y.; Kota, Y.; Iihama, S.; Suzuki, K.Z.; Sakuma, A.; Mizukami, S. Effect of Co and Fe Stoichiometry on Terahertz Emission from Ta/(Co_xFe_{1-x})₈₀B₂₀/MgO. *Phys. Rev. B* **2019**, *100*, 140406. [[CrossRef](#)]
51. Nenno, D.M.; Scheuer, L.; Sokoluk, D.; Keller, S.; Torosyan, G.; Brodyanski, A.; Lösch, J.; Battiato, M.; Rahm, M.; Binder, R.H.; et al. Modification of Spintronic Terahertz Emitter Performance through Defect Engineering. *Sci. Rep.* **2019**, *9*, 13348. [[CrossRef](#)]
52. Panahi, O.; Yahyaee, B.; Mousavi, S.M.; Ghiasabadi, A.M. High Performance Terahertz Emitter Based on Inverse Spin Hall Effect in Metallic Fe/Au Heterostructure. *Laser Phys.* **2020**, *30*, 055001. [[CrossRef](#)]
53. Zhang, S.; Jin, Z.; Zhu, Z.; Zhu, W.; Zhang, Z.; Ma, G.; Yao, J. Bursts of Efficient Terahertz Radiation with Saturation Effect from Metal-Based Ferromagnetic Heterostructures. *J. Phys. D Appl. Phys.* **2018**, *51*, 034001. [[CrossRef](#)]
54. Zhang, H.; Feng, Z.; Zhang, J.; Bai, H.; Yang, H.; Cai, J.; Zhao, W.; Tan, W.; Hu, F.; Shen, B.; et al. Laser Pulse Induced Efficient Terahertz Emission from Co/Al Heterostructures. *Phys. Rev. B* **2020**, *102*, 024435. [[CrossRef](#)]
55. Li, C.; Fang, B.; Zhang, L.; Chen, Q.; Xie, X.; Xu, N.; Zeng, Z.; Wang, Z.; Fang, L.; Jiang, T. Terahertz Generation via Picosecond Spin-to-Charge Conversion in IrMn₃/Ni-Fe Heterojunction. *Phys. Rev. Appl.* **2021**, *16*, 024058. [[CrossRef](#)]
56. Ni, Y.; Jin, Z.; Song, B.; Zhou, X.; Chen, H.; Song, C.; Peng, Y.; Zhang, C.; Pan, F.; Ma, G.; et al. Temperature-Dependent Terahertz Emission from Co/Mn₂Au Spintronic Bilayers. *Phys. Status Solidi Rapid Res. Lett.* **2021**, *15*, 2100290. [[CrossRef](#)]
57. Bierhance, G.; Markou, A.; Gueckstock, O.; Rouzegar, R.; Behovits, Y.; Chekhov, A.L.; Wolf, M.; Seifert, T.S.; Felser, C.; Kampfrath, T. Spin-Voltage-Driven Efficient Terahertz Spin Currents from the Magnetic Weyl Semimetals Co₂MnGa and Co₂MnAl. *Appl. Phys. Lett.* **2022**, *120*, 082401. [[CrossRef](#)]
58. Hawecker, J.; Rongione, E.; Markou, A.; Krishnia, S.; Godel, F.; Collin, S.; Lebrun, R.; Tignon, J.; Mangeney, J.; Boulier, T.; et al. Spintronic THz Emitters Based on Transition Metals and Semi-Metals/Pt Multilayers. *Appl. Phys. Lett.* **2022**, *120*, 122406. [[CrossRef](#)]

59. Heidtfield, S.; Adam, R.; Kubota, T.; Takanashi, K.; Cao, D.; Schmitz-Antoniak, C.; Bürgler, D.E.; Wang, F.; Greb, C.; Chen, G.; et al. Generation of Terahertz Transients from Co₂Fe_{0.4}Mn_{0.6}Si-Heusler-Alloy/Normal-Metal Nanobilayers Excited by Femtosecond Optical Pulses. *Phys. Rev. Res.* **2021**, *3*, 043025. [[CrossRef](#)]
60. Khang, N.H.D.; Ueda, Y.; Hai, P.N. A Conductive Topological Insulator with Large Spin Hall Effect for Ultralow Power Spin–Orbit Torque Switching. *Nat. Mater.* **2018**, *17*, 808–813. [[CrossRef](#)]
61. Hasan, M.Z.; Kane, C.L. Colloquium: Topological Insulators. *Rev. Mod. Phys.* **2010**, *82*, 3045–3067. [[CrossRef](#)]
62. Wang, X.; Cheng, L.; Zhu, D.; Wu, Y.; Chen, M.; Wang, Y.; Zhao, D.; Boothroyd, C.B.; Lam, Y.M.; Zhu, J.X.; et al. Ultrafast Spin-to-Charge Conversion at the Surface of Topological Insulator Thin Films. *Adv. Mater.* **2018**, *30*, 1802356. [[CrossRef](#)] [[PubMed](#)]
63. Tong, M.; Hu, Y.; Wang, Z.; Zhou, T.; Xie, X.; Cheng, X.; Jiang, T. Enhanced Terahertz Radiation by Efficient Spin-to-Charge Conversion in Rashba-Mediated Dirac Surface States. *Nano Lett.* **2021**, *21*, 60–67. [[CrossRef](#)] [[PubMed](#)]
64. Park, H.; Jeong, K.; Maeng, I.H.; Sim, K.I.; Pathak, S.; Kim, J.; Hong, S.B.; Jung, T.S.; Kang, C.; Kim, J.H.; et al. Enhanced Spin-to-Charge Conversion Efficiency in Ultrathin Bi₂Se₃ Observed by Spintronic Terahertz Spectroscopy. *ACS Appl. Mater. Interfaces* **2021**, *13*, 23153–23160. [[CrossRef](#)] [[PubMed](#)]
65. Park, H.; Rho, S.; Kim, J.; Kim, H.; Kim, D.; Kang, C.; Cho, M. Topological Surface-Dominated Spintronic THz Emission in Topologically Nontrivial Bi_{1-x}Sb_x Films. *Adv. Sci.* **2022**, *9*, 2200948. [[CrossRef](#)]
66. Cheng, L.; Wang, X.; Yang, W.; Chai, J.; Yang, M.; Chen, M.; Wu, Y.; Chen, X.; Chi, D.; Goh, K.E.J.; et al. Far Out-of-Equilibrium Spin Populations Trigger Giant Spin Injection into Atomically Thin MoS₂. *Nat. Phys.* **2019**, *15*, 347–351. [[CrossRef](#)]
67. Cong, K.; Vetter, E.; Yan, L.; Li, Y.; Zhang, Q.; Xiong, Y.; Qu, H.; Schaller, R.D.; Hoffmann, A.; Kemper, A.F.; et al. Coherent Control of Asymmetric Spintronic Terahertz Emission from Two-Dimensional Hybrid Metal Halides. *Nat. Commun.* **2021**, *12*, 5744. [[CrossRef](#)] [[PubMed](#)]
68. Seifert, T.S.; Tran, N.M.; Gueckstock, O.; Rouzegar, S.M.; Nadvornik, L.; Jaiswal, S.; Jakob, G.; Temnov, V.V.; Münzenberg, M.; Wolf, M.; et al. Terahertz Spectroscopy for All-Optical Spintronic Characterization of the Spin-Hall-Effect Metals Pt, W and Cu 80 Ir 20. *J. Phys. D Appl. Phys.* **2018**, *51*, 364003. [[CrossRef](#)]
69. Feng, Z.; Yu, R.; Zhou, Y.; Lu, H.; Tan, W.; Deng, H.; Liu, Q.; Zhai, Z.; Zhu, L.; Cai, J.; et al. Highly Efficient Spintronic Terahertz Emitter Enabled by Metal–Dielectric Photonic Crystal. *Adv. Opt. Mater.* **2018**, *6*, 1800965. [[CrossRef](#)]
70. Jin, Z.; Peng, Y.; Ni, Y.; Wu, G.; Ji, B.; Wu, X.; Zhang, Z.; Ma, G.; Zhang, C.; Chen, L.; et al. Cascaded Amplification and Manipulation of Terahertz Emission by Flexible Spintronic Heterostructures. *Laser Photon. Rev.* **2022**, *16*, 2100688. [[CrossRef](#)]
71. Nandi, U.; Abdelaziz, M.S.; Jaiswal, S.; Jakob, G.; Gueckstock, O.; Rouzegar, S.M.; Seifert, T.S.; Kläui, M.; Kampfrath, T.; Preu, S. Antenna-Coupled Spintronic Terahertz Emitters Driven by a 1550 Nm Femtosecond Laser Oscillator. *Appl. Phys. Lett.* **2019**, *115*, 022405. [[CrossRef](#)]
72. Shahriar, B.Y.; Carnio, B.N.; Hopmann, E.; Elezzabi, A.Y. Enhanced Directive Terahertz Radiation Emission from a Horn Antenna-Coupled W/Fe/Pt Spintronic Film Stack. *Appl. Phys. Lett.* **2021**, *119*, 092402. [[CrossRef](#)]
73. Hoppe, W.; Weber, J.; Tirpanci, S.; Gueckstock, O.; Kampfrath, T.; Woltersdorf, G. On-Chip Generation of Ultrafast Current Pulses by Nanolayered Spintronic Terahertz Emitters. *ACS Appl. Nano Mater.* **2021**, *4*, 7454–7460. [[CrossRef](#)]
74. Chen, M.; Wu, Y.; Liu, Y.; Lee, K.; Qiu, X.; He, P.; Yu, J.; Yang, H. Current-Enhanced Broadband THz Emission from Spintronic Devices. *Adv. Opt. Mater.* **2018**, *7*, 1801608. [[CrossRef](#)]
75. Liu, S.; Guo, F.; Li, P.; Wei, G.; Wang, C.; Chen, X.; Wang, B.; Zhao, W.; Miao, J.; Wang, L.; et al. Nanoplasmonic-Enhanced Spintronic Terahertz Emission. *Adv. Mater. Interfaces* **2022**, *9*, 2101296. [[CrossRef](#)]
76. Hibberd, M.T.; Lake, D.S.; Johansson, N.A.B.; Thomson, T.; Jamison, S.P.; Graham, D.M. Magnetic-Field Tailoring of the Terahertz Polarization Emitted from a Spintronic Source. *Appl. Phys. Lett.* **2019**, *114*, 031101. [[CrossRef](#)]
77. Gueckstock, O.; Nádvořník, L.; Seifert, T.S.; Borchert, M.; Jakob, G.; Schmidt, G.; Woltersdorf, G.; Kläui, M.; Wolf, M.; Kampfrath, T. Modulating the Polarization of Broadband Terahertz Pulses from a Spintronic Emitter at Rates up to 10 KHz. *Optica* **2021**, *8*, 1013. [[CrossRef](#)]
78. Agarwal, P.; Huang, L.; Ter Lim, S.; Singh, R. Electric-Field Control of Nonlinear THz Spintronic Emitters. *Nat. Commun.* **2022**, *13*, 4072. [[CrossRef](#)]
79. Kong, D.; Wu, X.; Wang, B.; Nie, T.; Xiao, M.; Pandey, C.; Gao, Y.; Wen, L.; Zhao, W.; Ruan, C.; et al. Broadband Spintronic Terahertz Emitter with Magnetic-Field Manipulated Polarizations. *Adv. Opt. Mater.* **2019**, *7*, 1900487. [[CrossRef](#)]
80. Chen, X.; Wu, X.; Shan, S.; Guo, F.; Kong, D.; Wang, C.; Nie, T.; Pandey, C.; Wen, L.; Zhao, W.; et al. Generation and Manipulation of Chiral Broadband Terahertz Waves from Cascade Spintronic Terahertz Emitters. *Appl. Phys. Lett.* **2019**, *115*, 221104. [[CrossRef](#)]
81. Cheng, H.; Huang, Q.; He, H.; Zhao, Z.; Sun, H.; Wu, Q.; Jiang, Z.; Wang, J.; Huang, H.; Fu, Z.; et al. Giant Electrical Modulation of Terahertz Emission in Pb(Mg_{1/3}Nb_{2/3})_{0.7}Ti_{0.3}O₃/Co-Fe-B/Pt. *Phys. Rev. Appl.* **2021**, *16*, 054011. [[CrossRef](#)]
82. Khusyainov, D.; Ovcharenko, S.; Buryakov, A.; Klimov, A.; Pernod, P.; Nozdrin, V.; Mishina, E.; Sigov, A.; Preobrazhensky, V.; Tiercelin, N. Composite Multiferroic Terahertz Emitter: Polarization Control via an Electric Field. *Phys. Rev. Appl.* **2022**, *17*, 044025. [[CrossRef](#)]
83. Seifert, T.; Jaiswal, S.; Sajadi, M.; Jakob, G.; Winnerl, S.; Wolf, M.; Kläui, M.; Kampfrath, T. Ultrabroadband Single-Cycle Terahertz Pulses with Peak Fields of 300 KV Cm⁻¹ from a Metallic Spintronic Emitter. *Appl. Phys. Lett.* **2017**, *110*, 252402. [[CrossRef](#)]
84. Milot, R.L.; Klug, M.T.; Davies, C.L.; Wang, Z.; Kraus, H.; Snaith, H.J.; Johnston, M.B.; Herz, L.M. The Effects of Doping Density and Temperature on the Optoelectronic Properties of Formamidinium Tin Triiodide Thin Films. *Adv. Mater.* **2018**, *30*, 1804506. [[CrossRef](#)] [[PubMed](#)]

85. Bai, Z.; Liu, Y.; Kong, R.; Nie, T.; Sun, Y.; Li, H.; Sun, T.; Pandey, C.; Wang, Y.; Zhang, H.; et al. Near-Field Terahertz Sensing of HeLa Cells and Pseudomonas Based on Monolithic Integrated Metamaterials with a Spintronic Terahertz Emitter. *ACS Appl. Mater. Interfaces* **2020**, *12*, 35895–35902. [[CrossRef](#)] [[PubMed](#)]
86. Balos, V.; Müller, P.; Jakob, G.; Kläui, M.; Sajadi, M. Imprinting the Complex Dielectric Permittivity of Liquids into the Spintronic Terahertz Emission. *Appl. Phys. Lett.* **2021**, *119*, 091104. [[CrossRef](#)]
87. Cheng, L.; Li, Z.; Zhao, D.; Chia, E.E.M. Studying Spin–Charge Conversion Using Terahertz Pulses. *APL Mater.* **2021**, *9*, 070902. [[CrossRef](#)]
88. Müller, M.; Martín Sabanés, N.; Kampfrath, T.; Wolf, M. Phase-Resolved Detection of Ultrabroadband THz Pulses inside a Scanning Tunneling Microscope Junction. *ACS Photonics* **2020**, *7*, 2046–2055. [[CrossRef](#)]
89. Chen, S.-C.; Feng, Z.; Li, J.; Tan, W.; Du, L.-H.; Cai, J.; Ma, Y.; He, K.; Ding, H.; Zhai, Z.-H.; et al. Ghost Spintronic THz-Emitter-Array Microscope. *Light Sci. Appl.* **2020**, *9*, 99. [[CrossRef](#)]
90. Bulgarevich, D.S.; Akamine, Y.; Talara, M.; Mag-usara, V.; Kitahara, H.; Kato, H.; Shiihara, M.; Tani, M.; Watanabe, M. Terahertz Magneto-Optic Sensor/Imager. *Sci. Rep.* **2020**, *10*, 1158. [[CrossRef](#)]
91. Guo, F.; Pandey, C.; Wang, C.; Nie, T.; Wen, L.; Zhao, W.; Miao, J.; Wang, L.; Wu, X. Generation of Highly Efficient Terahertz Radiation in Ferromagnetic Heterostructures and Its Application in Spintronic Terahertz Emission Microscopy (STEM). *OSA Contin.* **2020**, *3*, 893. [[CrossRef](#)]
92. Stiewe, F.-F.; Winkel, T.; Sasaki, Y.; Tubandt, T.; Kleinke, T.; Denker, C.; Martens, U.; Meyer, N.; Parvini, T.S.; Mizukami, S.; et al. Spintronic Emitters for Super-Resolution in THz-Spectral Imaging. *Appl. Phys. Lett.* **2022**, *120*, 032406. [[CrossRef](#)]
93. Agarwal, P.; Yang, Y.; Lourembam, J.; Medwal, R.; Battiato, M.; Singh, R. Terahertz Spintronic Magnetometer (TSM). *Appl. Phys. Lett.* **2022**, *120*, 161104. [[CrossRef](#)]